Research Square

Preprints are preliminary reports that have not undergone peer review.
They should not be considered conclusive, used to inform clinical practice,
or referenced by the media as validated information.

Neurotransmitter receptor-related signatures for prognostic stratification and immunotherapy response assessment in triple-negative breast cancer

Yixuan Wen
Shanghai East Hospital, School of Medicine, Tongji University
Jie Cui
Shanghai East Hospital, School of Medicine, Tongji University
Dong Xiang
The Affiliated Xuzhou Municipal Hospital of Xuzhou Medical University
Xingming Dai
The Affiliated Xuzhou Municipal Hospital of Xuzhou Medical University
Qi Li
Shanghai East Hospital, School of Medicine, Tongji University
Chunyan Dong
cy_dong@tongji.edu.cn

Shanghai East Hospital, School of Medicine, Tongji University

Article

Keywords: Triple-negative breast cancer, Neurotransmitter receptor-related genes, Machine learning, Prognosis, Immunotherapy response

Posted Date: November 23rd, 2026

DOI: https://doi.org/10.21203/rs.3.rs-11439969/v1

License: This work is licensed under a Creative Commons Attribution 4.0 International License.
Read Full License

Additional Declarations: No competing interests reported.

Neurotransmitter receptor-related signatures for prognostic stratification and immunotherapy response assessment in triple-negative breast cancer

Yixuan Wen[1+], Jie Cui[1+], Dong Xiang[2+], Xingming Dai[2], Qi Li[1*], Chunyan Dong[1*]

[1]Department of Oncology, Shanghai East Hospital, School of Medicine, Tongji University, Shanghai 200120, China

[2]Department of Bone and Joint Surgery and Sports Medicine, The Affiliated Xuzhou Municipal Hospital of Xuzhou Medical University, Xuzhou, Jiangsu, China

[+]These authors contributed equally to this work.

*Correspondence: Qi Li (qf.1007@163.com) and Chunyan Dong (cy_dong@tongji.edu.cn).

Abstract

Triple-negative breast cancer (TNBC) remains a major clinical challenge due to its pronounced heterogeneity and the lack of precise biomarkers. Here, we evaluated 101 machine-learning combinations across multi-cohort transcriptomic data to construct a Neurotransmitter Receptor-Related Signature (NRRS) comprising *CHRNA6*, *LY6E*, and *LY6H*. The NRRS was validated in external cohorts and showed prognostic value independent of clinical stage. Mechanistically, patients classified as high risk by the NRRS exhibited features of an "inflamed but immunosuppressive" microenvironment and higher T-cell dysfunction scores. Single-cell transcriptomic analysis further revealed that *CHRNA6* was enriched in regulatory T cells (Tregs) with enhanced immunosuppressive transcriptional features, *LY6E* was enriched in exhausted $CD8^+$ T cells ($CD8^+$ Tex) exhibiting features of terminal exhaustion, whereas *LY6H* was preferentially expressed in an endothelial subset with upregulated inflammation-associated genes and predicted immunosuppressive crosstalk involving MIF and SPP1 signaling. Together, these three cell-state signatures may contribute to the "inflamed but immunosuppressive" microenvironment. Notably, higher $CHRNA6^+$ Treg and $LY6E^+$ $CD8^+$ Tex signature scores were significantly associated with pathological complete response to atezolizumab plus chemotherapy, whereas the $LY6H^+$ endothelial signature was associated with poorer overall survival. These findings support the prognostic value of the NRRS and suggest that associated cell-state signatures may help identify patients more likely to respond to immunotherapy-containing regimens, offering a potential basis for personalized treatment in TNBC.

Keywords: Triple-negative breast cancer; Neurotransmitter receptor-related genes; Machine

learning; Prognosis; Immunotherapy response

Introduction

Triple-negative breast cancer (TNBC) is an aggressive subtype of breast cancer, defined by the absence of estrogen receptor, progesterone receptor, and human epidermal growth factor receptor 2 [1, 2]. Clinically, it accounts for approximately 15–20% of all breast cancers and is characterized by a pronounced peak of recurrence within the first 3–5 years, with a median overall survival (OS) of only 12–18 months once metastasis occurs [3, 4]. However, traditional anatomical staging systems may not fully capture prognostic heterogeneity due to the extensive molecular heterogeneity intrinsic to TNBC [5]. Despite recent advances in immunotherapy for TNBC, not all patients benefit, underscoring the need for biomarkers to identify those most likely to respond [6-8]. Therefore, there is an urgent need to develop novel molecular-based signatures to improve prognostic risk stratification and inform patient selection for immunotherapy.

Neurotransmitter receptors play critical roles in tumor initiation and progression [9]. Various neurotransmitter receptors are expressed by tumor cells and can modulate signaling pathways involved in proliferation, invasion, metastasis, and drug resistance [10-12]. Concurrently, neurotransmitter receptors can shape the tumor microenvironment (TME) by modulating the functions of T cells, macrophages, myeloid-derived suppressor cells (MDSCs), and dendritic cells, as well as influencing immune checkpoint expression. These effects can influence antitumor immunity and even contribute to immunotherapy resistance [13, 14]. Neurotransmitter receptor-related genes may serve as biomarkers of prognosis and immune status, and risk models based on neurotransmitter receptor-related genes have shown promising performance in several cancer types [15, 16]. However, their prognostic value, associated cellular expression patterns, and relevance to immunotherapy response in TNBC remain insufficiently characterized.

Here, we integrated machine learning with multi-cohort transcriptomic data (TCGA, GSE58812, and METABRIC) to construct a Neurotransmitter Receptor-Related Signature (NRRS) comprising *CHRNA6*, *LY6E*, and *LY6H*. The NRRS was validated in independent external cohorts, demonstrating independent prognostic value beyond conventional clinicopathological staging. Mechanistically, the high-risk phenotype was characterized by an "inflamed but immunosuppressive" microenvironment, potentially driven by *CHRNA6*$^{+}$ hyperactive regulatory T

cells (Tregs), *LY6E*$^{+}$ exhausted CD8^{+} T cells (CD8^{+} Tex) exhibiting features of terminal exhaustion, and *LY6H*$^{+}$ endothelial cell-mediated immunosuppressive crosstalk involving MIF and SPP1 signaling. Clinically, higher *CHRNA6*$^{+}$ Treg and *LY6E*$^{+}$ CD8^{+} Tex signature scores were significantly associated with higher pathological complete response (pCR) rates to atezolizumab plus chemotherapy, whereas the *LY6H*$^{+}$ endothelial signature was associated with poorer OS in the TCGA-TNBC cohort. In summary, these findings support the prognostic value of the NRRS and the potential of the associated T-cell signatures to inform response assessment for immunotherapy-containing regimens in TNBC.

Results

Machine learning identifies a neurotransmitter receptor-related prognostic signature in TNBC

PCA of the TCGA transcriptomic data revealed clear separation between TNBC and normal breast tissues (Figure 1A). Differential expression analysis using edgeR, DESeq2, and limma consistently identified 7,898 upregulated and 5,356 downregulated genes (Figure 1B). Given the emerging roles of neurotransmitter receptor signaling in tumor progression and the tumor microenvironment [9-11, 17], we intersected these DEGs with a curated neurotransmitter receptor-related gene set, yielding 66 overlapping candidate genes (Figure 1C), whose expression patterns are shown in Supplementary Figure 1. Subsequent univariate Cox regression analysis for OS identified 16 genes significantly associated with prognosis (Figure 1D). To construct a prognostic model, we systematically evaluated 101 machine-learning combinations based on 10 machine-learning algorithms. Model performance was assessed using 10-fold cross-validation, and the mean C-index across the TCGA, GSE58812, and METABRIC cohorts was used for model comparison. StepCox[both] + Ridge was among the highest-performing strategies (mean C-index = 0.652; Figure 1E) and initially retained four genes: *LY6E*, *CHRNA6*, *LY6H*, and *CHRM3*. The association of *CHRM3* with OS was not statistically significant in the multivariable Cox model (P = 0.099; Figure 1F), and the three- and four-gene models differed in AIC by 1.519. We therefore selected the more parsimonious three-gene signature comprising *CHRNA6*, *LY6H*, and *LY6E*, designated the NRRS. The Ridge regression coefficients (Figure 1G) defined the risk score as follows: Risk score = 0.898

× *CHRNA6* + 0.701 × *LY6H* + 0.485 × *LY6E*.

NRRS shows independent prognostic value and is associated with advanced clinical stage

We next assessed the prognostic value and clinical relevance of the NRRS across multiple TNBC cohorts. In the TCGA TNBC cohort, patients were ranked by increasing NRRS risk scores, with higher expression of the three constituent genes and a higher proportion of deaths observed in the high-risk group (Figure 2A). Kaplan-Meier survival analysis demonstrated significantly shorter OS in the high-risk group than in the low-risk group (Figure 2B). Time-dependent ROC analysis yielded AUCs of 0.837, 0.779, and 0.831 at 3, 6, and 9 years, respectively (Figure 2C). High-risk patients also showed significantly poorer survival in GSE58812 and METABRIC, both of which had been used for model selection and performance evaluation (Figures 2D and 2E). Furthermore, high-risk patients showed significantly poorer survival in two independent external TNBC cohorts not used for model development or selection, GSE135565 and GSE97342 (Figures 2F and 2G).

Univariate Cox regression identified significant associations of the NRRS risk score, T stage, N stage, M stage, and clinical stage with OS (Figure 2H). After adjustment for age and T, N, and M stage, the NRRS remained independently associated with OS ($P = 0.001$), as did N stage ($P < 0.001$) (Supplementary Figure 2). A nomogram incorporating the NRRS risk score and N stage was constructed to estimate 1-, 3-, and 5-year OS probabilities (Figure 2I). Age-category distributions did not differ significantly between the risk groups ($P = 1.000$), whereas clinical stage distributions differed ($P = 0.014$), with a higher proportion of stage III–IV disease in the high-risk group (Figure 2J).

The NRRS-defined high-risk group is linked to an inflamed yet immunosuppressive microenvironment with T-cell dysfunction

We next investigated the biological characteristics underlying the NRRS high-risk phenotype by profiling the transcriptomic signatures and immune landscape in the TCGA TNBC cohort. GSEA of GOCC and Hallmark gene sets revealed significant enrichment in immune- and inflammation-related signatures, including the T cell receptor complex, immunological synapses, interferon-γ-mediated responses, and the IL6-JAK-STAT3 signaling pathway (Figures 3A and 3B), suggesting enhanced immune and inflammatory activity within the high-risk group. Consistent with these enrichment results, the high-risk group exhibited significantly lower tumor purity (Figure 3C) and higher overall immune scores (Figure 3D), indicating an increased abundance of infiltrating immune

cells. Further single-sample GSEA (ssGSEA) analysis revealed specific immune infiltration profiles (Figure 3E). Notably, the high-risk group exhibited higher signature scores for activated lymphocytes (e.g., activated B cells and activated $CD8^+$ T cells), macrophage populations (M0, M1, and M2), and immunosuppressive cell populations such as MDSCs and Tregs. Additionally, T-cell co-inhibition and immune checkpoint signature scores were significantly higher in the high-risk group. We further evaluated the functional state of tumor-infiltrating T cells using the Tumor Immune Dysfunction and Exclusion (TIDE) scores (Figure 3F). Interestingly, while high-risk patients exhibited significantly higher $CD8^+$ T-cell and T-cell dysfunction scores, the exclusion scores and the overall TIDE scores showed no significant differences between the two groups. These findings suggest that T-cell dysfunction may contribute to immune evasion in the high-risk group. Consistent with this dysfunctional state, the expression of genes encoding key immune checkpoint molecules, including PD-1, CTLA4, LAG3, TIM-3, and VISTA, was markedly upregulated in the high-risk group (Figure 3G). In summary, the NRRS identifies a subset of TNBC patients harboring an inflamed yet immunosuppressive TME with concurrent T-cell dysfunction, which likely contributes to their unfavorable clinical outcomes.

The NRRS genes exhibit cell-type-specific expression patterns in the TNBC tumor microenvironment

To delineate the cellular context of the NRRS, the expression patterns of *LY6E*, *CHRNA6*, and *LY6H* were examined across two independent scRNA-seq cohorts. In the GSE161529 dataset, major cell types were identified and annotated using canonical marker genes (Figure 4A and Supplementary Figure 3A). Distinct distribution patterns emerged for the three genes (Figures 4B–4D). Specifically, *LY6E* exhibited widespread expression but showed the highest average expression in fibroblasts, followed by T cells. Meanwhile, *CHRNA6* was relatively enriched in T cells and macrophages, whereas *LY6H* was preferentially expressed in endothelial cells. These cell-type-specific patterns were further corroborated in the GSE305078 dataset, which showed broadly consistent cell-type enrichment patterns for all three genes (Figures 4E–4H and Supplementary Figure 3B).

Single-cell dissection reveals CHRNA6-associated immunosuppressive Treg features, *LY6E*-marked T-cell exhaustion, and *LY6H*-linked immunosuppressive signaling

Given the expression of *CHRNA6* and *LY6E* in T cells across both scRNA-seq cohorts, and the higher T-cell dysfunction scores in the NRRS-defined high-risk group, we further profiled the T-cell

compartment in the GSE305078 dataset. T-cell subclustering identified 8 distinct subtypes (Figure 5A). Notably, *CHRNA6* exhibited the highest expression in the Treg subset (Figure 5B). Compared with *CHRNA6*-negative Tregs, *CHRNA6*$^{+}$ Tregs exhibited significantly higher expression of CXCR3, TOX2, and TOLLIP, along with multiple immunosuppression-associated genes, including IKZF4, LGALS9, CCR8, HAVCR2, BTLA, TNFRSF25, and TNFAIP8L2 (Figure 5C). These findings suggest that *CHRNA6* identifies a Treg subpopulation characterized by an enhanced immunosuppressive transcriptional phenotype and activation-related transcriptional features. In parallel, *LY6E* showed the highest average expression in the CD8^{+} Tex subset (Figure 5D). Pseudotime trajectory analysis inferred a trajectory of CD8^{+} T cells toward terminal exhaustion (Figure 5E). Along the effector memory T-cell to Tex branch, LY6E expression varied non-monotonically and increased toward late pseudotime (Figure 5F). Additionally, *LY6E*$^{+}$ CD8^{+} Tex cells exhibited significantly higher expression of multiple exhaustion-associated genes, including CXCL13, LAG3, CTLA4, PDCD1, HAVCR2, and CD38 (Figure 5G). These results support an association between LY6E expression and an exhaustion-associated transcriptional state in CD8^{+} T cells.

Furthermore, *LY6H* marked an endothelial subset with inflammatory and immunosuppression-associated features. Compared with *LY6H*$^{-}$ endothelial cells, *LY6H*$^{+}$ endothelial cells exhibited significantly higher expression of immunosuppression-associated genes (CD276, VSIR, LGALS1, SPP1) and inflammation-associated genes (IL16, IL32, CCL14, CXCR4, AOC3, SEMA7A, NINJ1) (Figures 5H and 5I). Cell-cell communication analysis revealed markedly enhanced predicted outgoing signaling from *LY6H*$^{+}$ endothelial cells to other clusters compared with *LY6H*$^{-}$ cells (Supplementary Figures 4A and 4B). Specifically, this enhanced intercellular communication was predominantly mediated through the MIF and SPP1 signaling pathways (Figure 5J), suggesting that this endothelial subset may participate in immunoregulatory interactions within the TME.

These single-cell analyses depict a multi-layered immunosuppressive network: *CHRNA6* identifies a Treg population with activation-related and immunosuppression-associated transcriptional features; *LY6E* marks a late-stage exhausted state of CD8^{+} T cells; and *LY6H*$^{+}$ endothelial cells exhibit enhanced intercellular immunosuppressive crosstalk via MIF and SPP1 signaling. Collectively, these cellular states and intercellular interactions may contribute to the inflamed yet

immunosuppressive microenvironment characterized by T-cell dysfunction in the NRRS-defined high-risk group.

Linking cell-state signatures to immunotherapy response and prognostic stratification in TNBC

To assess the clinical relevance of the cell states identified above, we constructed three 15-gene signatures representing *CHRNA6*$^+$ Tregs, *LY6E*$^+$ CD8$^+$ Tex cells, and *LY6H*$^+$ endothelial cells. The corresponding scores distinguished marker-positive from marker-negative cells within each cell population in the single-cell dataset, with AUCs of 0.717, 0.723, and 0.906, respectively (Figures 6A–B, 6D–E, 6G–H). We next evaluated these signatures in an independent TNBC cohort treated with atezolizumab plus chemotherapy. High *CHRNA6*$^+$ Treg and *LY6E*$^+$ CD8$^+$ Tex signature scores were significantly associated with higher pCR rates (Figures 6C and 6F), highlighting their potential relevance to response to immunotherapy-containing treatment. In contrast, the *LY6H*$^+$ endothelial signature was not significantly associated with pCR (Figure 6I). Survival analysis in the TCGA-TNBC cohort revealed a different pattern. Neither the *CHRNA6*$^+$ Treg nor the *LY6E*$^+$ CD8$^+$ Tex signature showed a significant association with OS (Figures 6M and 6N), whereas high *LY6H*$^+$ endothelial signature scores were associated with significantly worse OS (Figure 6O). Together, these findings highlight the two T-cell signatures as potential markers of response to atezolizumab plus chemotherapy and the endothelial signature as a potential prognostic marker.

Finally, we examined the relationships between these cell-state signatures and the NRRS risk score. All three scores were positively correlated with NRRS risk score in the TCGA-TNBC cohort (Spearman's ρ = 0.250, 0.233, and 0.319, respectively; all $P < 0.01$; Figure 6J-L). Variance decomposition analysis further showed that the three signatures jointly explained 22.3% of the variance in the NRRS risk score (Total model R^2 = 22.3%; Supplementary Figure 4C), providing a cellular basis for the biological heterogeneity captured by the NRRS.

Protein expression and cellular localization of NRRS markers in TNBC tissues

To validate the NRRS markers at the protein level, we examined CHRNA6, LY6E, and LY6H expression in paired TNBC and adjacent non-tumorous tissues. Western blot analysis of five tissue pairs showed interpatient variation, with higher tumor expression of these proteins observed in several pairs (Figure 7A). Immunofluorescence analysis of a tissue microarray further revealed significantly higher percentages of CHRNA6-, LY6E-, and LY6H-positive cells in tumor tissues

than in adjacent tissues ($P = 0.017$, $P < 0.001$, and $P < 0.001$, respectively; Figure 7B). We next performed multiplex immunofluorescence staining to examine their cellular localization in TNBC tissue. CHRNA6 staining was detected in $CD4^+$ $FOXP3^+$ Tregs, LY6E staining in $CD8^+$ $PD\text{-}1^+$ T cells, and LY6H staining in $CD31^+$ endothelial cells (Figure 7C). These observations provide tissue-level support for the cellular expression patterns identified by single-cell transcriptomic analysis.

Discussion

Neurotransmitter receptors have been increasingly recognized as critical regulators of tumor progression and immune modulation, extending beyond their classical roles in the nervous system [9, 18-20]. However, the prognostic value of neurotransmitter receptor-related genes in TNBC remains largely underexplored, particularly regarding their potential to guide clinical decision-making.

In this study, we observed significant expression differences in neurotransmitter receptor-related genes between TNBC and normal tissues. To compare alternative modeling strategies, we screened 101 machine-learning combinations based on 10 machine-learning algorithms. Ten-fold cross-validation was used during model development, and models were compared using the mean C-index across the TCGA, GSE58812, and METABRIC cohorts. StepCox[both]–Ridge was among the highest-performing combinations and was selected for further model development. Based on this strategy, we constructed the NRRS comprising *LY6E*, *CHRNA6*, and *LY6H*. Consistent with the transcriptomic findings, tissue microarray analysis revealed higher proportions of CHRNA6-, LY6E-, and LY6H-positive cells in TNBC tissues than in adjacent tissues. Notably, during model refinement, we evaluated the initially retained fourth gene, *CHRM3*. Given its nonsignificant association with OS in multivariable Cox analysis and the small difference in AIC between models with and without this gene ($\Delta AIC = 1.519$), we excluded it to achieve a more parsimonious final model. Additionally, the NRRS demonstrated prognostic stratification in two independent external cohorts.

Multivariable Cox analysis further showed that the NRRS remained an independent predictor of OS after adjustment for age, T stage, N stage, and M stage, suggesting that our molecular signature provides complementary prognostic information beyond conventional clinicopathological parameters. Notably, clinical stage distribution differed significantly between the NRRS-defined

risk groups, with a higher proportion of stage III–IV disease in the high-risk group, indicating an association between higher NRRS scores and more advanced disease. These findings support the prognostic value of the NRRS in TNBC and its potential for future clinical application.

Accumulating evidence suggests that neurotransmitter receptors play an integral role in tumor immunity, influencing immune cell activation, polarization, and exhaustion and thereby shaping the tumor microenvironment [17, 21-24]. Here, we observed that high-risk patients exhibited an "inflamed but immunosuppressive" TME, with higher activated immune-cell signature scores alongside enrichment of MDSC and Treg signatures and increased expression of several immune checkpoint genes. Furthermore, TIDE analysis revealed higher T-cell dysfunction scores in the high-risk group, suggesting that T-cell dysfunction may contribute to immune evasion in these patients. These findings prompted us to investigate the cellular context of these immune features at the single-cell level, aiming to delineate the specific cell subsets that may contribute to the paradoxical microenvironment observed in high-risk TNBC.

Previous studies have suggested that *CHRNA6* may play a role in modulating immune responses and predicting immunotherapy outcomes in lung cancer [25, 26]. However, its cell-type-specific role within the TNBC microenvironment remains largely undefined. Using single-cell RNA-seq analysis, we found that *CHRNA6*$^+$ Tregs exhibited enhanced activation-related and immunosuppression-associated transcriptional features in TNBC. Similarly, *LY6E* was enriched in CD8$^+$ Tex, with *LY6E*$^+$ cells within this subset showing higher expression of classic exhaustion markers such as LAG3, CTLA4, and PDCD1. This is consistent with its known role as a T-cell exhaustion biomarker in systemic lupus erythematosus [27]. Further supporting these findings, multiplex immunofluorescence in TNBC tissue revealed cellular expression patterns consistent with those identified by single-cell analysis. More importantly, the specific enrichment of *CHRNA6*$^+$ Tregs or *LY6E*$^+$ Tex cells significantly predicted pCR to atezolizumab-combined chemotherapy, demonstrating that these gene-defined cell states can serve as effective biomarkers to identify patients most likely to benefit from immune checkpoint blockade.

Building on these findings, we further explored the transcriptional and signaling features of *LY6H*$^+$ endothelial cells. Notably, *LY6H*$^+$ endothelial cells exhibited stronger predicted outgoing MIF and SPP1 signaling, alongside upregulation of inflammation-associated genes, suggesting that they may contribute to an inflamed yet immunosuppressive tumor microenvironment. In terms of

clinical relevance, the *LY6H*$^{+}$ endothelial signature was not significantly associated with pCR to atezolizumab plus chemotherapy but was associated with poorer OS in the TCGA-TNBC cohort. Together, the cellular states represented by these three signatures may contribute to the inflamed but immunosuppressive tumor microenvironment and T-cell dysfunction observed in high-risk TNBC patients.

Despite these encouraging findings, several limitations should be considered. First, the transcriptomic datasets used for model construction and validation were retrospective, highlighting the need for prospective cohort studies to validate the clinical utility of the NRRS. Second, although the cell-state signatures were evaluated in an independent immunotherapy-treated cohort, the modest sample size and the uniform treatment regimen (atezolizumab plus chemotherapy) limit the extrapolation of these findings to other immunotherapeutic strategies. Third, although tissue analyses supported the protein expression and cellular localization of the NRRS markers, the proposed mechanisms remain largely based on single-cell bioinformatic analyses; therefore, functional experiments, such as in vivo models or CRISPR-based validation, are warranted to directly test the roles of these three genes in Treg-associated immunosuppression, T-cell exhaustion, and endothelial-mediated immunosuppression.

Overall, the NRRS provides prognostic stratification in TNBC, while the associated *CHRNA6*$^{+}$ Treg and *LY6E*$^{+}$ CD8^{+} Tex signatures show potential for identifying patients more likely to respond to atezolizumab plus chemotherapy.

Methods

Data collection

The TCGA-TNBC dataset was retrieved from the Genomic Data Commons (GDC) Data Portal (https://portal.gdc.cancer.gov/; accessed on 3 October 2025). Following selection based on TNBC status, 142 TNBC tumor samples and 113 normal breast tissue samples were included. Gene expression and survival data for the METABRIC cohort were retrieved from cBioPortal (https://www.cbioportal.org/). The TCGA-TNBC (n = 142), GSE58812 (n = 107; GPL570 platform), and METABRIC (n = 320) TNBC cohorts were used for model development and selection. Two additional independent TNBC cohorts, GSE97342 (n = 28) and GSE135565 (n = 84), were retrieved from the Gene Expression Omnibus (GEO) for external validation.

For immunotherapy response evaluation, the GSE319641 dataset, comprising 119 TNBC patients treated with atezolizumab plus chemotherapy, was retrieved from GEO. Of these patients, 63 achieved pCR, whereas 56 had residual disease.

For single-cell RNA sequencing (scRNA-seq) analysis, two publicly available datasets (GSE161529 and GSE305078) were retrieved from GEO. Eight TNBC samples from GSE161529 and 26 early-stage TNBC samples from GSE305078 were included. Raw count matrices were processed using the Seurat R package (v5.5.0). Cells with fewer than 200 or more than 6,000 detected genes, or mitochondrial counts exceeding 15% of total counts, were excluded. Doublets were identified and removed per sample using scDblFinder. Following log-normalization, the top 2,500 highly variable genes were selected for scaling and principal component analysis (PCA). The first 22 principal components (PCs) were used for Harmony batch correction, with sample identity as the batch variable. The Harmony-corrected embeddings were used to construct a shared nearest neighbor (SNN) graph. Cells were clustered using the Louvain algorithm and visualized using Uniform Manifold Approximation and Projection (UMAP). Cell-type annotation was based on canonical marker genes (Supplementary Figure 3). All single-cell analyses were conducted using R (version 4.6.0).

Differential expression analysis and neurotransmitter receptor-related gene selection

Differential expression analysis between TNBC and normal breast tissues in the TCGA cohort was performed using edgeR, DESeq2, and limma [28]. Genes with an $|\log_2 FC| > 0.585$ and a false discovery rate (FDR) < 0.05 were considered differentially expressed genes (DEGs). To define the neurotransmitter receptor-related gene set, we combined the "neurotransmitter receptor activity" gene set (GO:0030594) derived from the Molecular Signatures Database with a manually curated list of genes belonging to classical neurotransmitter receptor families annotated by the HUGO Gene Nomenclature Committee. After deduplication, 131 genes were retained (Supplementary Table S1). Genes overlapping between the consensus DEGs and this gene set were selected as candidates for subsequent analysis.

Construction and optimization of the machine learning-based risk signature

We systematically evaluated 101 combinations of 10 machine-learning algorithms: LASSO, Ridge, survival-SVM, Elastic Net, StepCox [both/forward/backward], CoxBoost, random survival forest [RSF], SuperPC, plsRcox, and GBM. Model performance was assessed via 10-fold cross-validation,

and models were compared using the mean concordance index (C-index) across the three discovery cohorts (TCGA, GSE58812, and METABRIC). StepCox[both] combined with Ridge regression was among the highest-performing combinations and was selected for model development. The risk score was calculated using the Ridge regression coefficients according to the following formula: Risk score = 0.898 × *CHRNA6* + 0.701 × *LY6H* + 0.485 × *LY6E*. Patients were stratified into low- and high-risk groups according to the median risk score.

Prognostic evaluation and survival analysis

OS was defined as the time from diagnosis to death or the last follow-up. Kaplan-Meier survival analysis was performed using the survival and survminer R packages, and differences between groups were evaluated using the log-rank test. Time-dependent receiver operating characteristic (ROC) curves were constructed using the timeROC R package to evaluate the prognostic performance of the NRRS at 3, 6, and 9 years. Univariate and multivariable Cox proportional hazards regression analyses were performed using the survival R package to evaluate the prognostic associations of the NRRS and clinicopathological factors (age, T stage, N stage, M stage, and clinical stage). A nomogram integrating the independent prognostic factors identified from the multivariable Cox analysis was constructed using the rms R package. Age and clinical stage distributions between the low- and high-risk groups were compared using Fisher's exact test.

Immune microenvironment characterization

Gene set enrichment analysis (GSEA) was performed using the clusterProfiler R package to identify enriched Gene Ontology Cellular Component (GOCC) and Hallmark gene sets between the low- and high-risk groups. Normalized enrichment scores and FDR-adjusted P-values were calculated. Tumor purity and immune scores were estimated using the ESTIMATE algorithm [29]. Additionally, immune cell signature enrichment scores were calculated by single-sample GSEA (ssGSEA) using the GSVA R package to characterize relative immune infiltration. The Tumor Immune Dysfunction and Exclusion (TIDE) algorithm was used to estimate T-cell dysfunction and exclusion scores and the overall TIDE score [30].

Single-cell RNA-seq trajectory and cell-cell communication analysis

For the GSE305078 dataset, the T-cell compartment was extracted and re-clustered to distinguish specific T-cell subtypes (e.g., Tregs, $CD8^+$ Tex). Pseudotime trajectory analysis was conducted using the Monocle R package to infer the state transition of $CD8^+$ T cells toward exhaustion. For cell-cell

communication analysis, the CellChat R package was employed to infer the intercellular communication networks based on the expression of known ligand-receptor pairs. Differences in signaling pathways between *LY6H*$^{+}$ and *LY6H*$^{-}$ endothelial cells were compared to dissect the potential immunosuppressive roles associated with *LY6H*.

To identify the transcriptional features of the specific cell subpopulations, differential expression analysis was performed using the FindMarkers function from the Seurat R package. Specifically, differential expression was assessed separately between *CHRNA6*$^{+}$ and *CHRNA6*$^{-}$ Tregs, *LY6E*$^{+}$ and *LY6E*$^{-}$ CD8^{+} Tex cells, and *LY6H*$^{+}$ and *LY6H*$^{-}$ endothelial cells. The Wilcoxon rank-sum test was used for differential expression analysis, and genes with an absolute $\log_2$ fold change ($|\log_2 FC|$) greater than 0.25 and an adjusted P-value (Bonferroni correction) less than 0.05 were considered significantly differentially expressed.

Construction of cell-state signatures and variance decomposition

To quantify the transcriptomic divergence of specific cell subpopulations, 15-gene signature scores were constructed by calculating the average expression of marker genes specifically upregulated in *CHRNA6*$^{+}$ Tregs, *LY6E*$^{+}$ CD8^{+} Tex cells, and *LY6H*$^{+}$ endothelial cells. The marker gene lists for each subpopulation are provided in Supplementary Table S2. The discriminative ability of each signature was assessed via ROC curve analysis within the scRNA-seq dataset. The contributions of these three cell-state signatures to the overall prognostic variance were assessed using variance decomposition analysis (relative importance analysis) via the relaimpo R package. The total model R^2 was decomposed to quantify the independent explanatory power of each cell-state signature.

Western blot analysis

Paired tumor and adjacent non-tumorous tissues from five patients with TNBC were obtained from the Department of Breast Surgery, Shanghai East Hospital, School of Medicine, Tongji University, with approval from the hospital's Ethics Committee (No. 2026YS-064). Western blot analysis was performed on tissue lysates using primary antibodies against CHRNA6 (Proteintech, China, 11388-1-AP), LY6E (Cell Signaling Technology, USA, 37690), and LY6H (Proteintech, China, 23933-1-AP). GAPDH (Proteintech, China, 60004-1-Ig) was used as a loading control. Band intensities were quantified using ImageJ software and normalized to the corresponding GAPDH band intensities.

Multiplex immunofluorescence staining and analysis

Multiplex immunofluorescence staining was performed on a commercial tissue microarray

(Shanghai Outdo Biotech, China; tissue microarray ID: TNBC1602) and tissue sections from a patient with TNBC. The tissue microarray was stained for CHRNA6, LY6E, and LY6H. The patient-derived sections were stained using three panels: CHRNA6/CD4/FOXP3, LY6E/CD8/PD-1, and LY6H/CD31. The following primary antibodies were used: CHRNA6 (Invitrogen, USA, MA5-31689), LY6E (GeneTex, USA, GTX637770), LY6H (Abcam, UK, ab55472), CD4 (Abcam, UK, ab133616), FOXP3 (Abcam, UK, ab20034), CD8 (Abcam, UK, ab17147), PD-1 (Abcam, UK, ab137132), and CD31 (Abcam, UK, ab28364).

Following deparaffinization, rehydration, antigen retrieval, and blocking, tissue sections were stained with the primary antibodies and fluorescent detection reagents. Nuclei were counterstained with DAPI, and slides were mounted with an antifade mounting medium. Fluorescence images were analyzed using SelvanViewer software. For tissue microarray quantification, the number of marker-positive cells was expressed as a percentage of the total number of DAPI-positive cells.

Statistical analysis

All statistical analyses were performed using R (version 4.6.0). Continuous variables between two groups were compared using the Wilcoxon rank-sum test. Categorical variables were compared using the Chi-square test or Fisher's exact test. Correlation analyses between continuous variables were conducted using Spearman's rank correlation. A two-sided $P < 0.05$ was considered statistically significant. P-values were adjusted to control the FDR or using Bonferroni correction, as specified for the corresponding analyses.

Data availability

TCGA data were obtained from the Genomic Data Commons Data Portal (https://portal.gdc.cancer.gov/), and METABRIC data were obtained from cBioPortal (https://www.cbioportal.org/). The bulk and single-cell transcriptomic datasets are available from the Gene Expression Omnibus (https://www.ncbi.nlm.nih.gov/geo/) under accession numbers GSE58812, GSE97342, GSE135565, GSE319641, GSE161529, and GSE305078. Gene sets and gene annotations were obtained from the Molecular Signatures Database (https://www.gsea-msigdb.org/gsea/msigdb/) and the HUGO Gene Nomenclature Committee database (https://www.genenames.org/).

Code availability

The analysis code is available from the corresponding authors upon reasonable request.

References

1. Brenton, J.D., et al., *Molecular classification and molecular forecasting of breast cancer: ready for clinical application?* Journal of Clinical Oncology : Official Journal of the American Society of Clinical Oncology, 2005. **23**(29): p. 7350–7360.
2. Foulkes, W.D., I.E. Smith, and J.S. Reis-Filho, *Triple-negative breast cancer.* The New England Journal of Medicine, 2010. **363**(20): p. 1938–1948.
3. Dent, R., et al., *Triple-negative breast cancer: clinical features and patterns of recurrence.* Clinical Cancer Research : an Official Journal of the American Association For Cancer Research, 2007. **13**(15 Pt 1): p. 4429–4434.
4. Waks, A.G. and E.P. Winer, *Breast Cancer Treatment: A Review.* JAMA, 2019. **321**(3): p. 288–300.
5. Asleh, K., N. Riaz, and T.O. Nielsen, *Heterogeneity of triple negative breast cancer: Current advances in subtyping and treatment implications.* Journal of Experimental & Clinical Cancer Research : CR, 2022. **41**(1): p. 265.
6. Schmid, P., et al., *Overall Survival with Pembrolizumab in Early-Stage Triple-Negative Breast Cancer.* The New England Journal of Medicine, 2024. **391**(21): p. 1981–1991.
7. Cortes, J., et al., *Pembrolizumab plus Chemotherapy in Advanced Triple-Negative Breast Cancer.* The New England Journal of Medicine, 2022. **387**(3): p. 217–226.
8. Mittendorf, E.A., et al., *Neoadjuvant atezolizumab in combination with sequential nab-paclitaxel and anthracycline-based chemotherapy versus placebo and chemotherapy in patients with early-stage triple-negative breast cancer (IMpassion031): a randomised, double-blind, phase 3 trial.* Lancet (London, England), 2020. **396**(10257): p. 1090–1100.
9. Wang, X., et al., *Cancer and neurotransmitter receptors.* Chinese Medical Journal, 2025. **138**(13): p. 1540–1558.
10. Tu, R.-H., et al., *Neurotransmitter Receptor HTR2B Regulates Lipid Metabolism to Inhibit Ferroptosis in Gastric Cancer.* Cancer Research, 2023. **83**(23): p. 3868–3885.
11. Jiang, S.-H., et al., *GABRP regulates chemokine signalling, macrophage recruitment and tumour progression in pancreatic cancer through tuning KCNN4-mediated Ca2+ signalling in a GABA-independent manner.* Gut, 2019. **68**(11): p. 1994–2006.
12. Huang, D., et al., *Cancer-cell-derived GABA promotes β-catenin-mediated tumour growth and immunosuppression.* Nature Cell Biology, 2022. **24**(2): p. 230–241.
13. Zhang, C., et al., *The neuro-immune axis in cancer: from mechanisms to therapeutic opportunities.* Journal of Hematology & Oncology, 2025. **18**(1): p. 93.
14. Yang, J., et al., *Neurotransmitters: an emerging target for therapeutic resistance to tumor immune checkpoint inhibitors.* Molecular Cancer, 2025. **24**(1): p. 216.
15. Zhang, W., et al., *Systematic Analysis of Neurotransmitter Receptors in Human Breast Cancer Reveals a Strong Association With Outcome and Uncovers HTR6 as a Survival-Associated Gene Potentially Regulating the Immune Microenvironment.* Frontiers In Immunology, 2022. **13**: p. 756928.

16. Zhang, L., et al., *Neurotransmitter receptor-related gene signature as potential prognostic and therapeutic biomarkers in colorectal cancer.* Frontiers In Cell and Developmental Biology, 2023. **11**: p. 1202193.
17. Fan, M. and X. Zhao, *Role of the neurotransmitter-receptor pathway in T-cell tumor immunology and cancer immunotherapy.* Acta Biochimica Et Biophysica Sinica, 2025. **58**(1): p. 67–89.
18. Li, R.Q., et al., *Exploring neurotransmitters and their receptors for breast cancer prevention and treatment.* Theranostics, 2023. **13**(3): p. 1109–1129.
19. Yang, M.-W., et al., *Perineural Invasion Reprograms the Immune Microenvironment through Cholinergic Signaling in Pancreatic Ductal Adenocarcinoma.* Cancer Research, 2020. **80**(10): p. 1991–2003.
20. Chen, Y., et al., *Dopamine Signaling Promotes Tissue-Resident Memory Differentiation of CD8+ T Cells and Antitumor Immunity.* Cancer Research, 2022. **82**(17): p. 3130 – 3142.
21. Karmakar, S. and G. Lal, *Role of serotonin receptor signaling in cancer cells and anti-tumor immunity.* Theranostics, 2021. **11**(11): p. 5296–5312.
22. Zhang, C., et al., *The role of acetylcholine and its receptors in tumor immune regulation: mechanisms and potential therapeutic targets.* Molecular Cancer, 2025. **24**(1): p. 231.
23. Globig, A.-M., et al., *The β1-adrenergic receptor links sympathetic nerves to T cell exhaustion.* Nature, 2023. **622**(7982): p. 383–392.
24. Park, H.-J., S.-C. Lee, and S.-H. Park, *Norepinephrine stimulates M2 macrophage polarization via β2-adrenergic receptor-mediated IL-6 production in breast cancer cells.* Biochemical and Biophysical Research Communications, 2024. **741**: p. 151087.
25. Zhang, F., et al., *Involvement of CHRNA6 in the Immune Response in Lung Squamous Cell Carcinoma and its Potential as a Drug Target for the Disease.* Current Pharmaceutical Design, 2023. **29**(26): p. 2091–2100.
26. Zhao, Q., et al., *Potential immunologic and prognostic roles of CHRNA6 in SCLC and pan-cancer.* Heliyon, 2024. **10**(19): p. e38572.
27. Zheng, Y., et al., *Identification and immunoassay of biomarkers associated with T cell exhaustion in systemic lupus erythematosus.* Frontiers In Immunology, 2025. **16**: p. 1476575.
28. Liu, S., et al., *Three Differential Expression Analysis Methods for RNA Sequencing: limma, EdgeR, DESeq2.* Journal of Visualized Experiments : JoVE, 2021(175).
29. Yoshihara, K., et al., *Inferring tumour purity and stromal and immune cell admixture from expression data.* Nature Communications, 2013. **4**: p. 2612.
30. Jiang, P., et al., *Signatures of T cell dysfunction and exclusion predict cancer immunotherapy response.* Nature Medicine, 2018. **24**(10): p. 1550–1558.

Acknowledgments

This work was supported by the following funding programs: Shanghai Leading Talent Program of Eastern Talent Plan (No. DFYCLJ02); New Quality Clinical Specialty Program of High-end Medical Disciplinary Construction in Shanghai Pudong New Area (No. 2025-PWXZ-01); Shanghai Pudong New Area Health Commission Investigator-Initiated Clinical Research Project (No. 2026-

PWDL-02)；Tongji University Interdisciplinary Program in Clinical Medicine (No. 2025-0345-ZD-02); Beijing Science and Technology Innovation Medical Development Fund (No. KC2023-JX-0288-BZ84); Xuzhou Health Commission Young Talent Program for Medical Science and Technology Innovation (No. XWKYHT20240089); Development Fund of the Affiliated Hospital of Xuzhou Medical University (No. XYFM202444).

Author contributions

Q.L. and C.D. conceived and supervised the study. Y.W. and J.C. performed the bioinformatic analyses and experiments and drafted the manuscript. D.X. contributed to data analysis and interpretation. X.D. collected clinical samples and performed experiments. Q.L. and C.D. critically revised the manuscript. All authors reviewed and approved the final manuscript.

Competing interests

The authors declare no competing interests.

Figures and Figure legends

Figure 1.

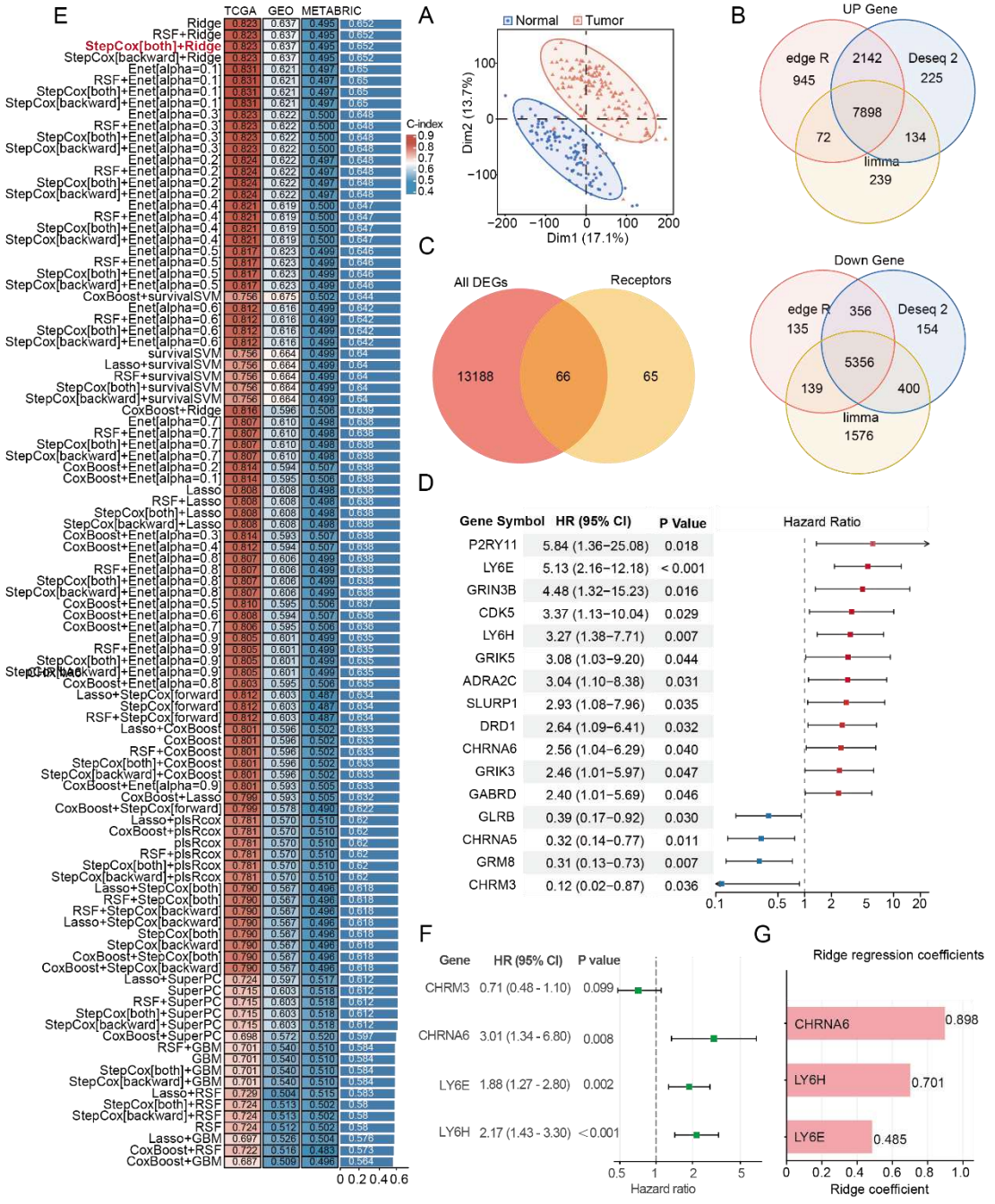


Figure 1. Identification of a neurotransmitter receptor-related prognostic signature in TNBC via machine learning.

(A) Principal component analysis (PCA) of 142 TNBC and 113 normal breast tissue samples from the TCGA database. (B) Venn diagrams showing the overlap of upregulated and downregulated differentially expressed genes (DEGs) identified using edgeR, DESeq2, and limma ($|\log_2 FC| > 0.585$,

FDR < 0.05). (C) Venn diagram showing the intersection of the consensus DEGs with a neurotransmitter receptor-related gene set. (D) Forest plot showing the 16 prognostically significant genes ($P < 0.05$) selected from 66 candidate neurotransmitter receptor-related genes by univariate Cox regression for overall survival (OS). (E) Heatmap summarizing the C-index values of 101 machine learning combinations. Columns correspond to the TCGA, GSE58812, and METABRIC cohorts, while rows correspond to the distinct algorithm combinations. (F) Forest plot showing the multivariable Cox regression analysis of the four machine learning-selected candidate genes. (G) Bar plot illustrating the Ridge coefficients of the three genes incorporated into the final risk model.

Figure 2.

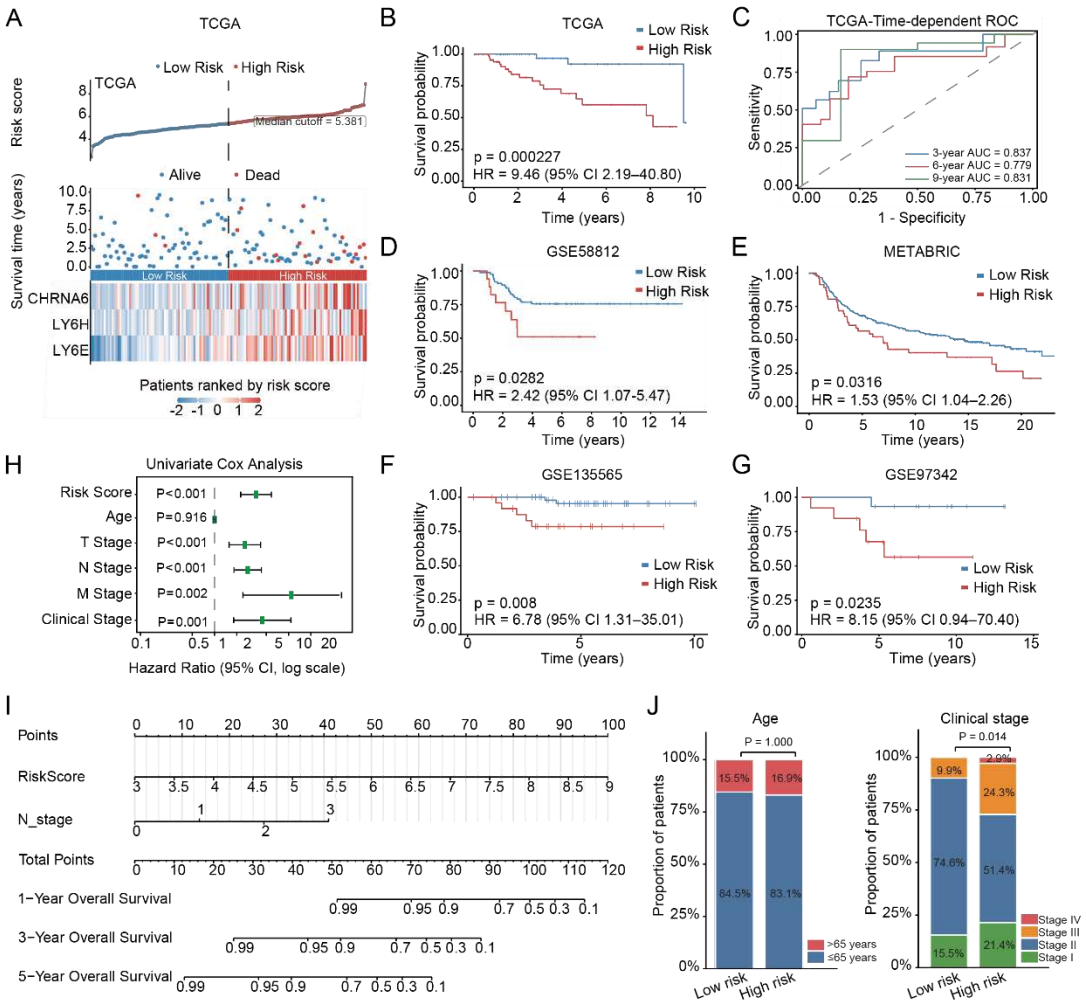


Figure 2. Prognostic evaluation and clinical relevance of the NRRS in TNBC.

(A) Ranking of patients by increasing NRRS risk score in the TCGA-TNBC cohort, with corresponding survival status and an expression heatmap of *CHRNA6*, *LY6H*, and *LY6E*. (B) Kaplan–Meier curves for OS in the TCGA-TNBC cohort (n=142). (C) Time-dependent ROC curves for 3-, 6-, and 9-year OS in the TCGA-TNBC cohort. (D, E) Kaplan–Meier curves for OS in the GSE58812 (n=107) and METABRIC (n=320) TNBC cohorts, respectively. (F, G) Kaplan–Meier curves for OS in the GSE135565 (n = 84) and GSE97342 (n = 28) independent external TNBC cohorts, respectively. (H) Forest plot displaying the univariate Cox regression analysis of the risk score and clinicopathological factors. (I) Nomogram integrating the risk score and N stage for predicting 1-, 3-, and 5-year OS probabilities. (J) Stacked bar charts displaying the distributions of age (>65 vs. ≤65 years) and clinical stage (stages I–IV) between low- and high-risk groups.

Figure 3.

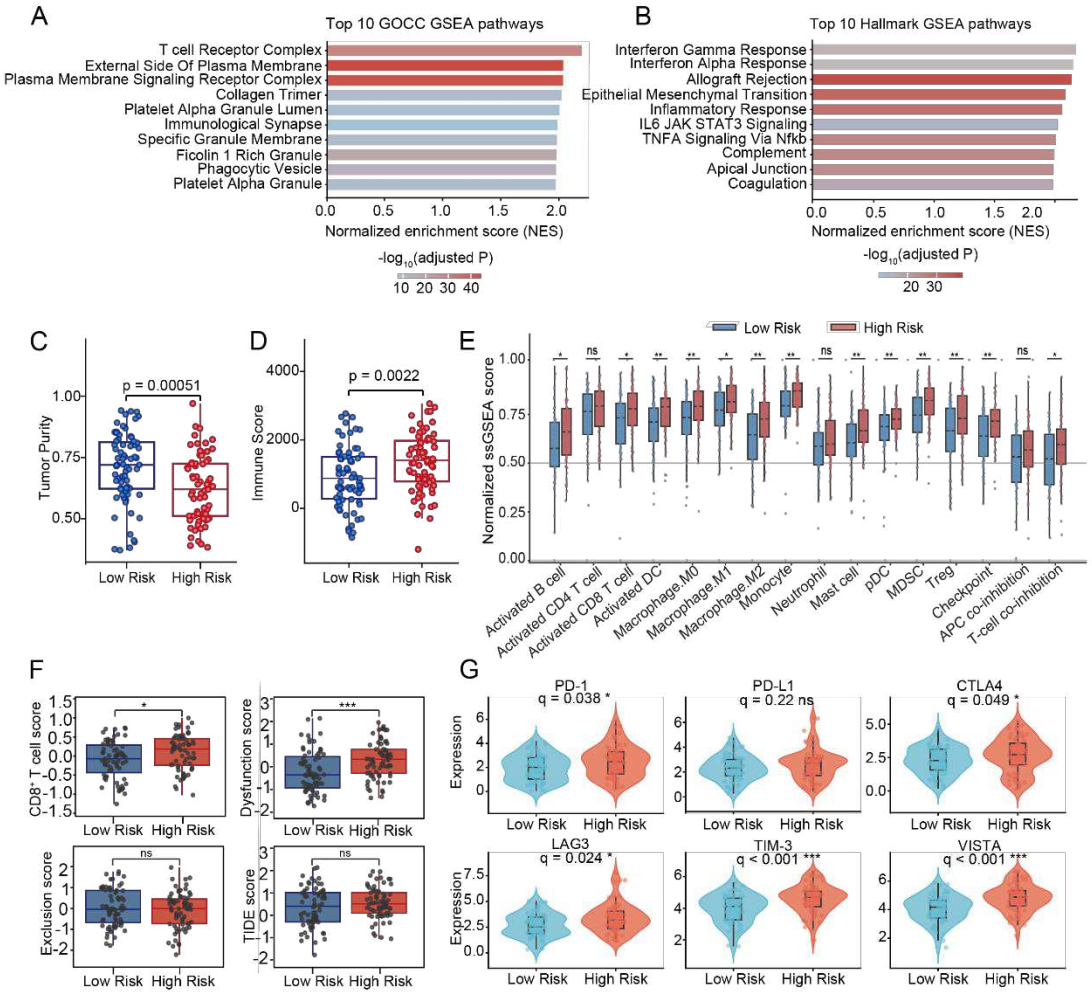


Figure 3. The NRRS-defined high-risk group is associated with an inflamed yet immunosuppressive microenvironment and T-cell dysfunction.

(A, B) Top 10 enriched Gene Ontology Cellular Component (GOCC) and Hallmark gene sets in the high-risk group, respectively, revealed by GSEA. Bar length indicates the normalized enrichment score (NES), and bar color represents $-\log_{10}$(adjusted P). (C, D) Comparison of tumor purity and immune infiltration scores between low- and high-risk groups. (E) Normalized single-sample GSEA (ssGSEA) scores of immune cell subsets and immunoregulatory pathways between low- and high-risk groups. (F) Comparison of TIDE-derived $CD8^+$ T cell, dysfunction, exclusion, and overall Tumor Immune Dysfunction and Exclusion (TIDE) scores between low- and high-risk groups. (G) Expression of genes encoding key immune checkpoint molecules, with FDR-adjusted P values (q values) indicated. All analyses were performed in the TCGA-TNBC cohort. ns, not significant; *P < 0.05; **P < 0.01; ***P < 0.001

Figure 4.

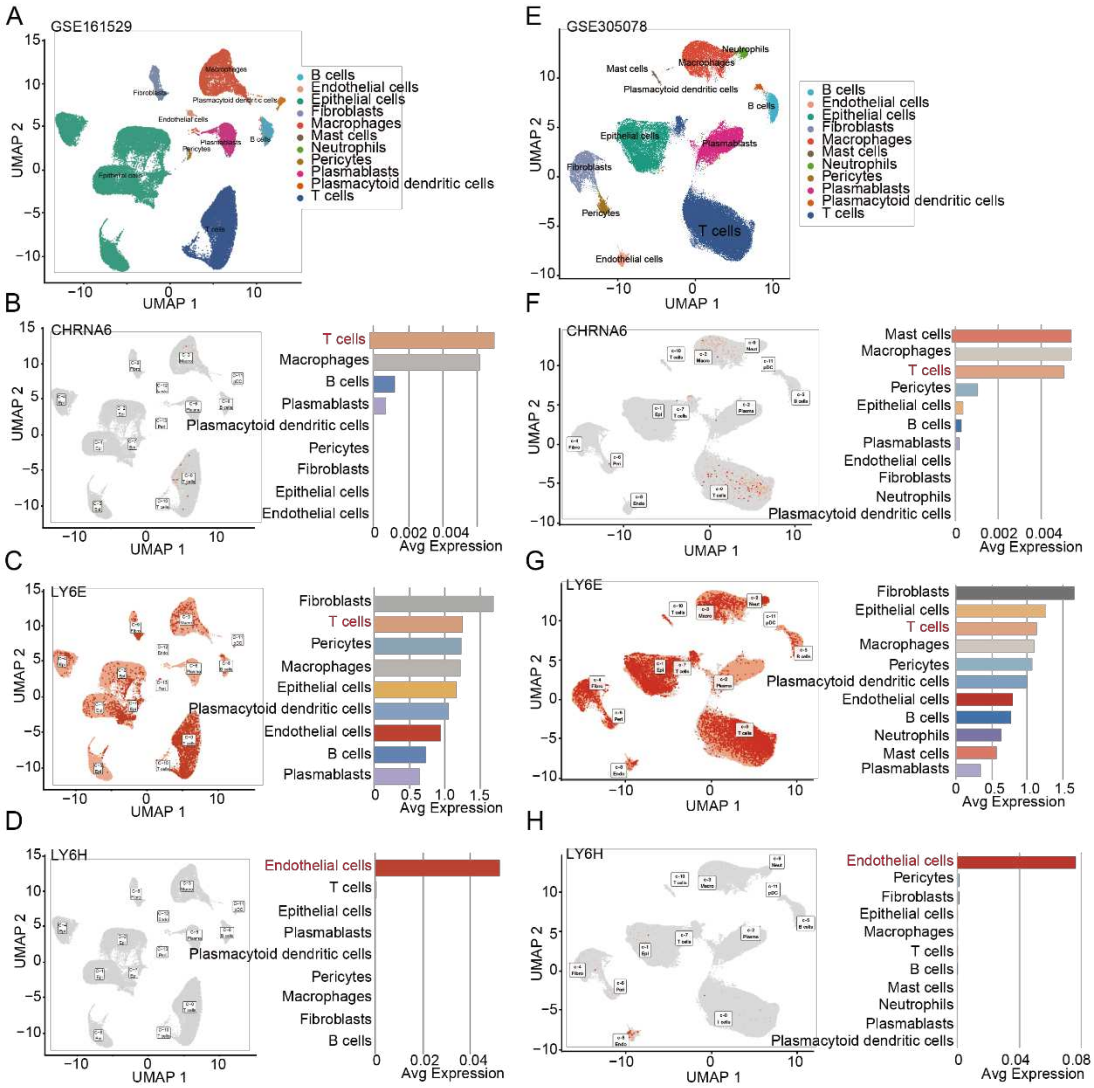


Figure 4. Cell-type-specific expression patterns of the NRRS genes in the TNBC microenvironment.

(A) UMAP visualization of annotated major cell types in the GSE161529 scRNA-seq cohort. (B–D) Feature plots displaying the expression distributions and bar plots showing the corresponding average expression levels of *CHRNA6* (B), *LY6E* (C), and *LY6H* (D) across distinct cell types in the GSE161529 cohort. (E) UMAP visualization of annotated major cell types in the GSE305078 scRNA-seq cohort. (F–H) Expression distribution and corresponding average expression levels of *CHRNA6* (F), *LY6E* (G), and *LY6H* (H) across distinct cell types in the GSE305078 cohort.

Figure 5.

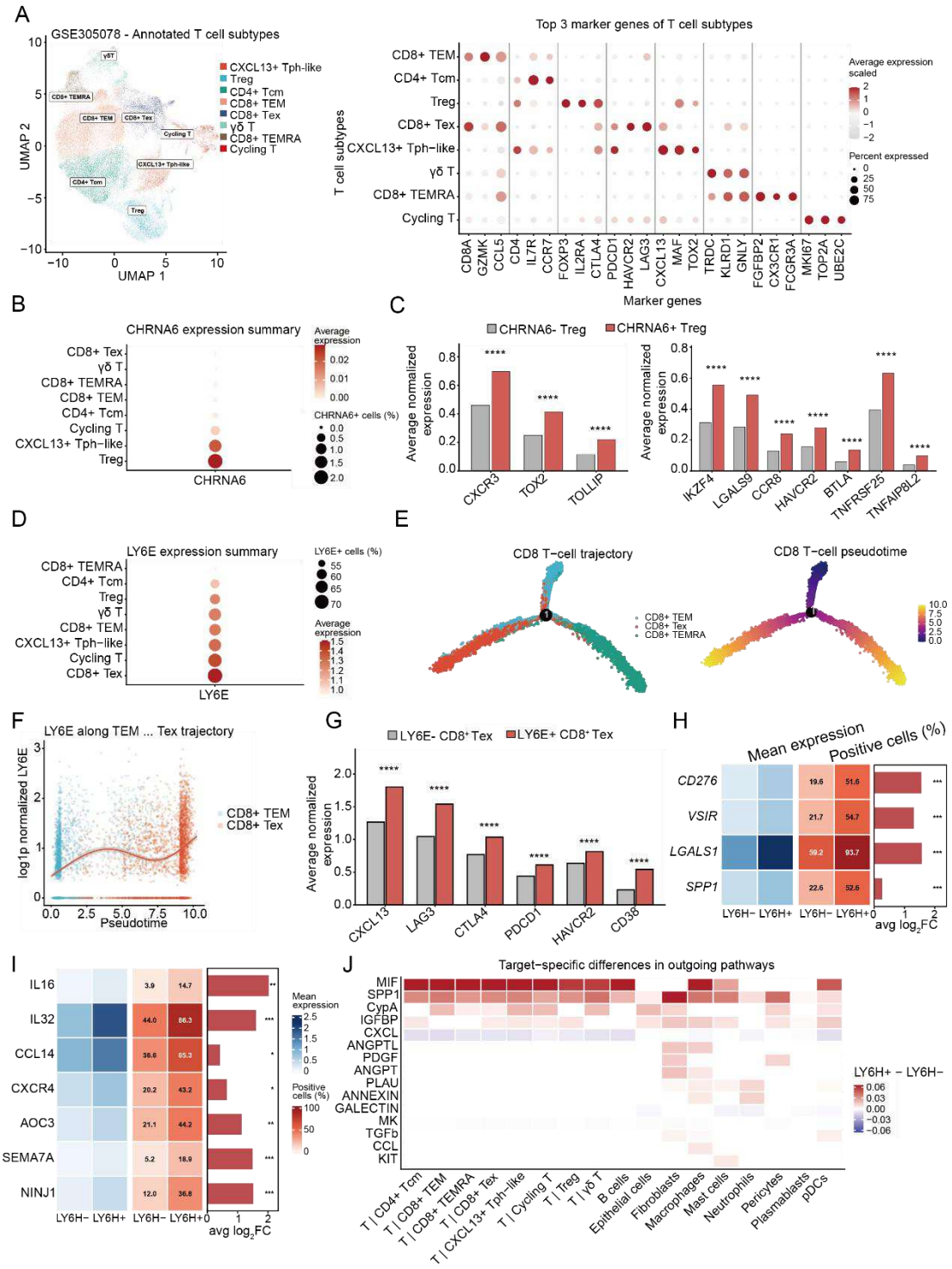


Figure 5. Single-cell characterization of NRRS-associated cell states and predicted intercellular signaling.

(A) T-cell subclustering and expression of three marker genes for each subtype in the GSE305078 cohort. (B) *CHRNA6* expression profiles across T-cell subtypes. (C) Differential expression of

activation-related and immunosuppression-associated genes in *CHRNA6*$^{+}$ versus *CHRNA6*$^{-}$ Tregs. (D) *LY6E* expression profiles across T-cell subtypes. (E) Pseudotime trajectory inference of CD8^{+} T cells. (F) *LY6E* expression dynamics along the CD8^{+} T-cell exhaustion trajectory. (G) Expression levels of exhaustion markers between *LY6E*$^{+}$ and *LY6E*$^{-}$ CD8^{+} Tex cells. (H) Expression levels and percentages of expressing cells for immunosuppression-associated genes in *LY6H*$^{+}$ versus *LY6H*$^{-}$ endothelial cells. (I) Expression levels of inflammation-associated genes in *LY6H*$^{+}$ versus *LY6H*$^{-}$ endothelial cells. (J) Outgoing signaling pathway differences from *LY6H*$^{+}$ compared with *LY6H*$^{-}$ endothelial cells to other cell clusters. *P < 0.05; **P < 0.01; ***P < 0.001; ****P < 0.0001

Figure 6.

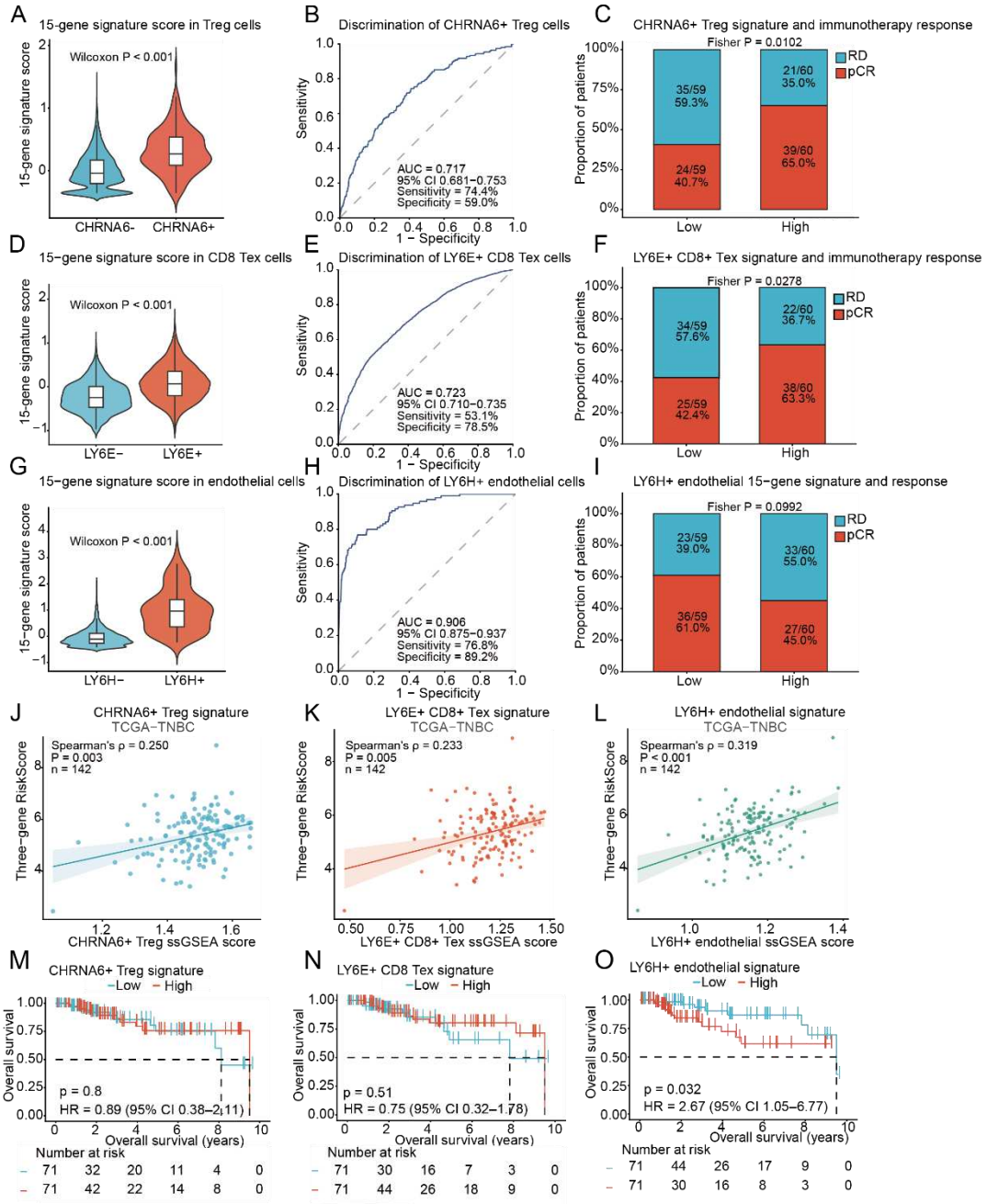


Figure 6. Associations of cell-state signatures with immunotherapy response, survival, and NRRS risk scores.

(A, D, G) Comparison of 15-gene signature scores between *CHRNA6*$^{+}$ and *CHRNA6*$^{-}$ Tregs, *LY6E*$^{+}$ and *LY6E*$^{-}$ CD8^{+} Tex cells, and *LY6H*$^{+}$ and *LY6H*$^{-}$ endothelial cells, respectively. (B, E, H) ROC curves evaluating the ability of the corresponding 15-gene signatures to distinguish marker-positive from marker-negative cell subsets. (C, F, I) Comparison of pathological complete response (pCR) and residual disease (RD) rates between low- and high-score groups for the corresponding

signatures in an independent TNBC cohort treated with atezolizumab plus chemotherapy. (J, K, L) Spearman's correlation analyses between the three cell-state signature scores and the NRRS risk score in the TCGA-TNBC cohort (n=142), with ρ and P-values indicated. (M, N, O) Kaplan–Meier curves for OS in the TCGA-TNBC cohort according to low and high scores for the *CHRNA6*$^{+}$ Treg, *LY6E*$^{+}$ CD8^{+} Tex, and *LY6H*$^{+}$ endothelial signatures, respectively.

Figure 7.

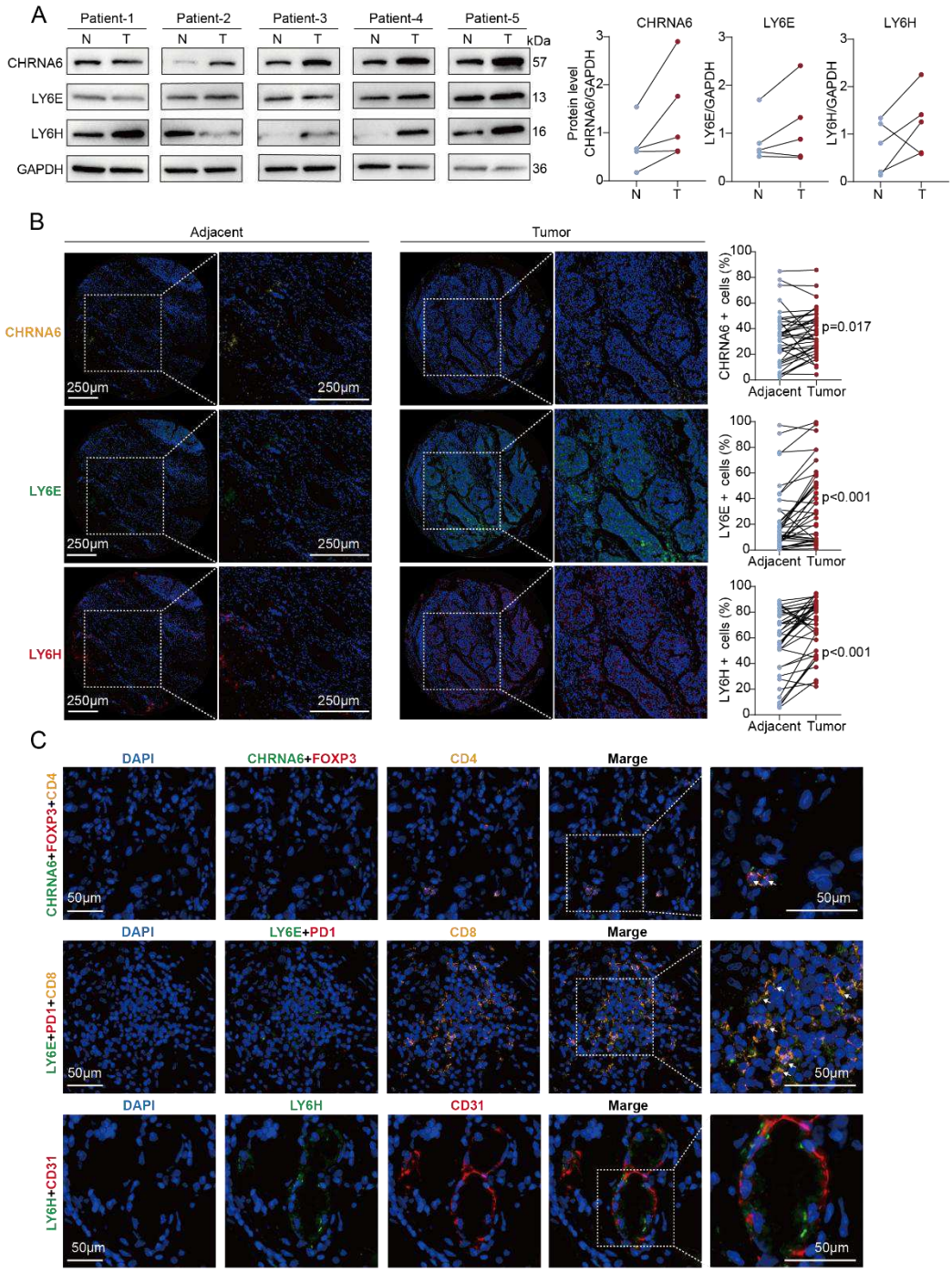


Figure 7. Protein expression and cellular localization of NRRS markers in TNBC tissues.

(A) Western blot analysis and quantification of CHRNA6, LY6E, and LY6H in paired tumor (T) and adjacent non-tumorous (N) tissues from five patients with TNBC. Protein levels were normalized to GAPDH. (B) Representative immunofluorescence images and percentages of CHRNA6-, LY6E-, and LY6H-positive cells in paired tumor and adjacent tissues from a tissue microarray. (C)

Representative multiplex immunofluorescence images showing CHRNA6 staining in $CD4^+FOXP3^+$ Tregs, LY6E staining in $CD8^+PD\text{-}1^+$ T cells, and LY6H staining in $CD31^+$ endothelial cells in TNBC tissue. Scale bars are indicated in the images.

Supplementary Files

This is a list of supplementary files associated with this preprint. Click to download.

- SupplementaryInformation.pdf
- UncroppedWesternBlotsFigure7A.pdf